Two-channel Epidermal RFID Sensor for the Wireless Bilateral Analysis of Nasal Respiration

Nicoletta Panunzio, *Student Member, IEEE*, Elisa Fontana, Francesco Montecchia, and Gaetano Marrocco, *Senior Member, IEEE*

***Abstract*— Abnormal breathing can be a symptom of an unhealthy status. Conventional diagnostic exams involve cumbersome and intrusive instrumentation, such as nasal cannulas, that is uncomfortable for the user and that, most of the times, do not consider the breathing asymmetries between the two nostrils. This paper describes a two-channel flexible epidermal sensor for the wireless and less-invasive bilateral monitoring of nasal breathing based on temperature measurement. The device is suitable to adhere to the prolabium, and comprises two coupled T-match antennas whose Ultra High Frequency (UHF) Radio Frequency IDentification (RFID) ICs are placed at the entrance of the nostrils. They are provided with embedded temperature sensors, so that they implement both sensing and transmission of the data. A measurement campaign is carried out to provide a *quantitative* characterization of the dual-channel device as a breath sensor by comparison with a conventional flow meter. The two nostrils can be independently monitored due to a negligible cross-sensitivity of the two ICs' temperature data. Moreover, temperature-based measurements proved capable to reproduce typical clinical breathing features, with less than 12% uncertainty with respect to flow waveforms.**

***Index Terms*— RFID, epidermal antenna, temperature sensor, breath monitoring, respiratory flow, flow meter**

I. Introduction

BREATH monitoring is an essential clinical procedure for the early diagnosis of respiratory and cardiovascular diseases [1], [2]. In particular, breath rate, peaks of respiratory cycles, and their duration are common indicators for the identification and monitoring of breathing disorders, such as the Chronic Obstructive Pulmonary Disease (COPD) [3] and the recent SARS-COV-2 illness [4], as well as for the follow-up of patients. Since the nasal cavities work differently during a respiratory cycle, even in the absence of pathologies, a bilateral measure of nostrils' breath may provide further deeper insight. This is the case of temporary obstruction or permanent deviation of the nasal septum.

Breathing is typically monitored by means of spirometry [5] that measures the respiratory flows and accordingly estimates the respiratory rates, volumes, and secondary parameters. Spirometry requires the patient to breathe in a controlled manner while wearing uncomfortable nasal or mouth *cannulas* connected to a flow meter. This test can be performed only in hospitals with the supervision of an expert operator.

To avoid such discomfort, wireless wearable technologies may provide an attractive alternative [6]. The breath information is indirectly extracted by collecting the moisture or the temperature gradients that are produced during inhalation and exhalation by means of physical/chemical transducers such as graphite ink [7], [8], PEDOT:PSS loading [9], thermistors [10], [11], and platinum films anemometer [12]. Above devices are generally bulky, include complex electronics, and communicate by using a BLE (Bluetooth Low Energy) interface, so that a local power source is required. They hence involve limitations for real-life application that instead demands comfort, simplicity, and easy disposal, which means no batteries onboard.

Battery-less Radiofrequency Identification (RFID) technology, coupled with Epidermal Electronics [13], can hence boost the development of low-invasive, low-cost, and ease-of-use devices for breath measurement. The required power for the sensor is provided wirelessly by an external reader working in the Ultra High Frequency (UHF) RFID frequency band (860-960 MHz). Data transmission from the sensor to the reader exploits instead *zero-power* communication through modulated backscattering. The pioneering experiments in [14] and [15] involved a moisture-sensitive RFID device that was equipped with an external graphene-oxide electrode. But, this electronic complexity can be minimized by resorting to temperature-based monitoring of breath. Indeed, the fresher ambient air entering the nostrils and the warm air coming out from the lungs produce a rhythmic sequence of decrements (inhalation) and restoration (exhalation) of temperature, that can be correlated to the respiratory acts. Hence, the RFID devices in [16] only involve the solid-state temperature sensor that is embedded into the RFID Integrated Circuit (IC) itself. In this way, the resulting devices provide both identification, sensing, and transmission with just a single IC, so that the overall size is limited and the expected total cost is compatible with disposable usage. Preliminary attempts to achieve a bilateral measurement of breathing can be found in [17], where

The work was developed in the framework of the Dual-Skin project, funded by *Italian Ministry of University and Research* (FISR 2020 COVID, Ref. FISR2020IP 00227).

Nicoletta Panunzio, Elisa Fontana, and Gaetano Marrocco are with the Pervasive Electromagnetics Lab, University of Rome Tor Vergata, 00133 Roma, Italy (e-mail: nicoletta.panunzio@uniroma2.it, elisa-fontana2001@gmail.com, gaetano.marrocco@uniroma2.it).

Francesco Montecchia is with the Civil Engineering and Computer Science Engineering Department, University of Rome Tor Vergata, 00133 Roma, Italy (e-mail: francesco.montecchia@uniroma2.it).

the authors proposed two tapered epidermal loops, inductively coupled with a smaller loop probe hosting the IC. However, the device was cumbersome, not easy to attach, remove, and place again on the skin. Moreover, it was verified only for communication but not for the true sensing of breath.

Overall, concerning the clinical insight of the collected data, all the above-cited papers mainly focus on the respiration rate, while instead other relevant breathing features are under-investigated. In particular, temperature-based breath monitoring via RFID epidermal sensors has been only *qualitatively* demonstrated. Hence, a true *quantitative* analysis of the clinical meaningfulness of the achieved results with respect to more assessed and conventional techniques is still in question.

By expanding the preliminary conference paper in [18], this contribution faces the above challenges by *quantitatively* characterizing, for the first time, a two-channel RFID-based breath sensor in comparison with a clinical-grade flow-meter. The RFID device for the tests is improved with respect to the state of the art as it is now made by soft and adhesive biocompatible elastomeric compounds that permit a more comfortable adhesion on the skin and the possibility of reusing the sensor by the same patient. The goal is to evaluate the capability of the RFID sensor to monitor the two nostrils independently and, above all, to reproduce the typical clinical parameters of breath, and hence to quantify the *level of agreement* with a conventional equipment.

The paper is organized into two parts. The first one is devoted to the design and electromagnetic characterization of the dual-channel RFID-based soft sensor. The simulation model and numerical analysis are described in Section II. Indeed, as two ICs are required below the nostrils, the epidermal sensor includes two electromagnetically coupled ports [19]. Moreover, they are also influenced by the *auto-tuning* behavior of the considered ICs, that automatically adjust their internal impedance to maximize the wireless power transfer [20]. Fabrication and experimental characterization of the device are then presented in Section III. The second part of the paper is instead dedicated to the quantitative characterization of the dual-channel device as a breath sensor. In particular, Section IV introduces the experimental set-up and the breath features to be measured, whereas Section V outlines the data-processing procedure. Finally, the results of a measurement campaign on some healthy volunteers are analyzed in Section VI by means of a statistical approach.

II. Modeling and Design of the Flexible and Soft Epidermal Sensor

A. Layout

The dual-tag bilateral breath sensor consists of two T-match asymmetric dipoles (Fig. 1.a), suitable to be attached over the prolabium and arranged in a symmetric configuration with respect to the sagittal plane of the face. Each antenna is made of an aluminum trace ($s = 2\ mm$), cut out from a COTS inlay tag by Axzon [21] to ease the fabrication. Indeed, the size $H = 1.2cm$ in the lip-to-nose direction is compatible with the average anatomic size (0.5–1.5cm [22]), as well as the size $W = 0.8\ cm$ that is compatible with the cross-section of the nostrils outlet. Hence, the device can fit over the prolabium. The size L was instead adjusted in simulation to optimize the performance of the device on the face.

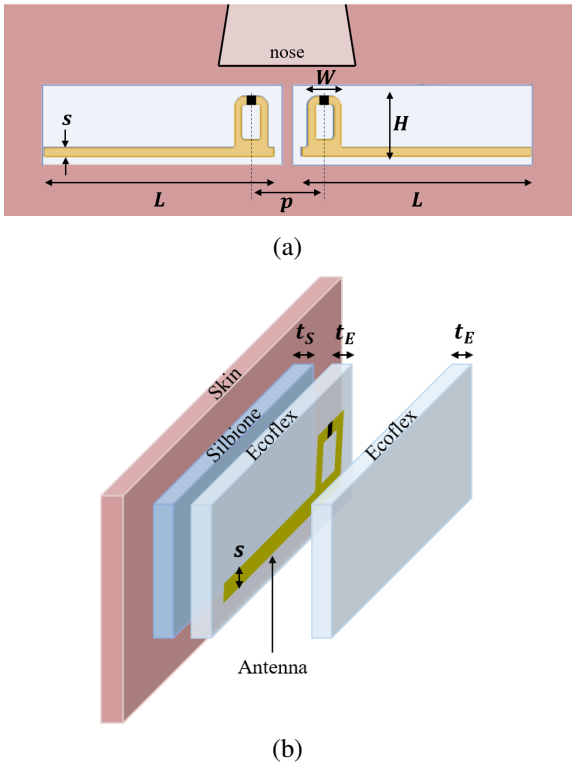

Fig. 1. (a) Layout of the dual-tag epidermal antenna. (b) Exploded view of the encapsulating elastomeric layers.

To make the sensor soft and comfortable for the user, the antenna is packaged with elastomeric coatings (Fig. 1.b). The metal traces are sandwiched between two layers of Ecoflex^{TM}($t_E = 0.3\ mm$, $\varepsilon = 2.7$, $\sigma = 0.007\ S/m$), and the adhesion on the skin is provided by a softer layer of Silbione^{TM}($t_S = 0.2\ mm$, $\varepsilon = 2.5$, $\sigma = 0.0012\ S/m$). The overall thickness of the device is less than $1\ mm$.

B. RFID Auto-Tuning IC Transponder

The considered IC transponder is the Axzon Magnus-S3 [23], having a nominal chip sensitivity $p_{chip} = -16.6\ dBm$. It is provided with the *auto-tuning* technology [20] that automatically adjusts its internal impedance to maximize the harvested power. The IC hence acts as a variable load with input admittance $Y_{IC} = G_{IC} + j\omega C_{IC}$. The capacitance $C_{IC} = C_{IC,0} + sC_{IC,step}$ is adjusted by an internal varactor within a given range[1] to enforce the resonance condition $|B_A^{in} + \omega C_{IC}| = 0$, being B_A^{in} the input susceptance of the antenna. In this way, the power transfer coefficient between the antenna and the IC is maximized at $\tau = 4G_{IC}G_A^{in}/|G_{IC} + G_A^{in}|^2$, as well as the realized gain $\tilde{G} = \tau G$, where G is the antenna radiation gain. The realized gain is directly related to the maximum achievable reading distance, whenever the activation condition $P_{R\to T} \geq p_{chip}$ is satisfied.

[1]Parameters of the IC: $G_{IC} = 0.482\ mS$, $C_{IC,0} = 1.9\ pF$, $C_{IC,step} = 1.96\ fF$ and $0 \leq s \leq 511$ [23].

The selected IC is also provided with an embedded solid-state temperature sensor, allowing the minimization of required electronic components and costs. It has an operating range of $-40°C \leq T \leq 85°C$ and resolution of $0.13°C$ [23], but, since the temperature data are retrieved from the voltage measurement of a p-n junction inside the IC, they can be affected by the impinging RF signal when it overcomes a given threshold, thus reducing accuracy and precision. According to the datasheet, the temperature measurement can be considered valid only when the value of the Power-on-Chip (PoC) Code[2] falls within the range $13 \leq PoC \leq 18$, whereas non-linear effects arise for larger values. This range is here extended by means of the power-based correction in [24], so that reliable temperature data are returned for $13 \leq PoC \leq 30$. In this way, the measurements are insensitive to the interrogation modalities, and the achievable accuracy and precision are $0.2°C$. The lower bound $PoC \geq 13$, instead, determines the maximum temperature-reading distance, which is generally lower than that in case of identification only.

C. Electromagnetic Model

As the two T-match loops hosting the ICs are placed very close to each other ($p = 1.6\,cm$ in Fig. 1.a), the electromagnetic coupling is inevitably established between them. Hence, the two antennas must be considered as a two-port symmetric system [25] with self (S) and mutual (M) admittances $Y_{S/M} = G_{S/M} + jB_{S/M}$. Nevertheless, each *auto-tuning* IC connected to the ports still adjusts its internal impedance to maximize the harvested power. So, the resonance condition will be enforced at each port, becoming $|B_n^{in} + \omega C_{IC,n}| = 0$ [19], where B_n^{in} is the input susceptance of the n-th port for the specific arrangement. It is worth noticing that, depending on the type of the established coupling (i.e., constructive or destructive), improvements over the single-port case may be achieved, which result in a power transfer coefficient that can exceed unity [25]. This means that each antenna is "helping" the harvesting of the other.

In case of coupled multi-*auto-tuning*-chip systems, the realized gain is expressed as in [19], [25]:

$$\tilde{G}_n = 4\eta_0 G_{IC,n} |[\mathbf{Y_G^{-1}}]_n \cdot \mathbf{g}|^2 , \tag{1}$$

where η_0 is the impedance of the vacuum, $\mathbf{g}$ is the column vector of the normalized port gains, which groups the parameters of the system, whereas $[\mathbf{Y_G^{-1}}]_n$ indicates the n-th row of the inverse of the system admittance matrix $\mathbf{Y_G} = \mathbf{Y} + \mathbf{Y_{IC}}$, being $\mathbf{Y}$ the two-port system matrix and $\mathbf{Y_{IC}} = diag(Y_{IC,1}, Y_{IC,2})$ the ports termination matrix (for detailed formulation see [19]).

By exploiting the symmetry, and provided that a broadside interrogation is performed [19], the realized gain reduces to the standard expression:

$$\tilde{G}_{L/R} = \tau_{L/R}\, G_{L/R} , \tag{2}$$

where $G_{L/R}$ is the radiation gain referred to the left (L) and right (R) ports when the other is short-circuited, and $\tau_{L/R}$ is the power transfer coefficient between each coupled antenna and its IC [19], [20]:

$$\tau_{L/R} = \frac{4 G_{IC} G_S}{|G_{IC} + G_S + G_M|^2} . \tag{3}$$

[2]The PoC Code is a 5-bit value $\in [0, 31]$ returned by the IC during a standard RFID interrogation, indicating the amount of power collected by the IC.

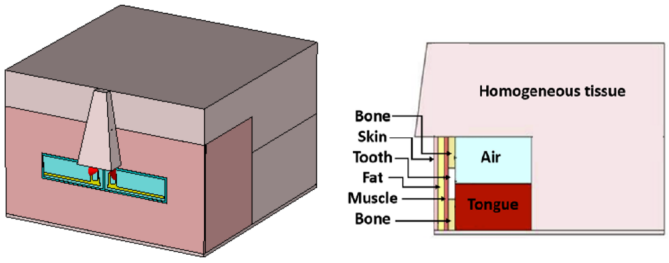

(a) (b)

Fig. 2. (a) Simplified numerical phantom of the eyes-to-chin human head. (b) Details of the stratification of the model. Size and dielectric properties as in [17].

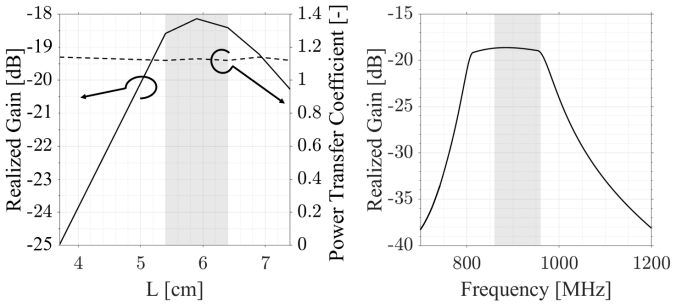

(a) (b)

Fig. 3. (a) Simulated realized gain and power transmission coefficient at $\boldsymbol{f = 868}$ MHz versus the length $\boldsymbol{L}$ of the dipole placed over the phantom as in Fig. 2. Shadowed, the range corresponding to less than $\mathbf{1}\ \boldsymbol{dB}$ reduction from the peak value of realized gain. (b) Simulated frequency behavior of the realized gain for $\boldsymbol{L = 5.4\ cm}$. Shadowed, the Worldwide UHF band.

D. Numerical Simulations

1) Numerical Head Phantom: For design purpose, electromagnetic simulations are performed by using CST Microwave Studio 2018. The dual-tag device is accommodated over a simplified multi-layer model of the human head (Fig. 2), borrowed from [17].

2) Parametric Analysis: The parameter L is varied in simulations between $3.7\,cm$ and $7.4\,cm$ to determine the optimal length for the maximum realized gain and power transfer coefficient in the broadside direction, computed as in Eq. (2) and (3). Fig. 3.a shows that, thanks to a constructive coupling, the power transfer coefficient exceeds unity and is quite constant for every choice of L. Instead, the peak of the realized gain falls in the range $5.4\,cm \leq L \leq 6.4\,cm$. The size $L = 5.4\,cm$ is selected to minimize the antenna footprint. The corresponding realized gain $\tilde{G}_{L/R} = -18.5\,dB$ is comparable with typical performance of on-skin antennas [26]. Thanks to the auto-tuning, the frequency profile (Fig. 3.b) is rather flat in the worldwide RFID band. By assuming the reader emits the maximum power of $3.2\,W\ EIRP$ allowed by European regulations [27], the estimated maximum read distance is little lower than $60\,cm$.

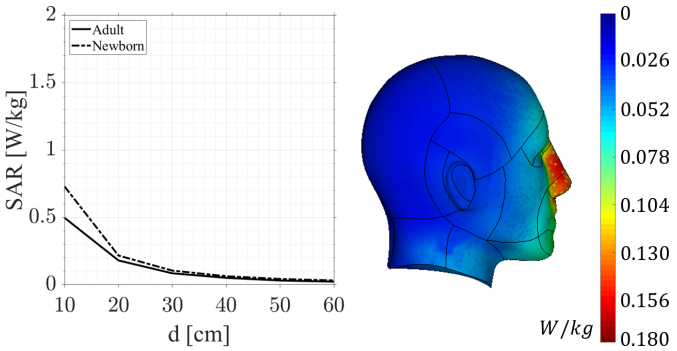

(a) (b)

Fig. 4. (a) Peak value of the SAR varying the antenna-face distance. (b) Example of SAR simulation results in case of the adult head for an antenna-face distance of $\mathbf{20}\ \boldsymbol{cm}$.

3) Safety Issues: According to safety regulations [28], the Specific Absorption Rate (SAR) must be less than $2\,W/kg$ for head and trunks, averaged over $10\,g$ of tissues and time-averaged over 6 minutes of exposure. A simulation was performed to assess the SAR. The numerical phantom of the human head was this time an anthropomorphic model[3] (inset of Fig. 4) with homogeneous dielectric properties ($\varepsilon = 42.7, \sigma = 0.99\,S/m$ [29]), that was also rescaled by 63% to emulate the size of a newborn's head. To replicate a typical interrogating antenna used in realistic operating conditions, a $11\ cm \times 11\ cm$ circularly polarized patch as in [30] was considered in simulation, again emitting $3.2\,W\ EIRP$. The interrogator was placed at a variable distance d from the faces to replicate a worst-case scenario in which the interrogation is continuous with a unitary duty cycle. The peak value of the SAR averaged over $10\,g$ of tissue is shown in Fig. 4 for each antenna-face distance, in case of both the adult and the newborn heads. In all the cases, the SAR is far below the limit, hence providing flexibility for a safe practical setup, even in case of long-term exposure, when needed.

III. Prototypes and Electromagnetic Measurement

A. Prototypes

A prototype of the dual-channel breath sensor is shown in Fig. 5. It was manufactured [31] by using a rectangular mold, with a bumper at the chip position, to leave it uncovered by the elastomeric coatings so as to be more sensitive to temperature gradients generated by breathing. Both Ecoflex^{TM} and Silbione^{TM} compounds were prepared by mixing their two sub-components in equal quantity for 3 minutes; then, the resulting mixture was degassed ($-1\ atm$) for 2 minutes to remove air bubbles. After that, the manufacturing procedure involved the following sequential steps: *(i)* covering the mold by a layer of spray releaser (to ease the removal of the prototypes), *(ii)* pouring a $0.3\ mm$ layer of Ecoflex^{TM}, *(iii)* depositing the aluminum T-match dipole and pouring another $0.3\,mm$ layer of Ecoflex^{TM}, *(iv)* spreading a $0.2\,mm$ Silbione^{TM} layer. After each coating deposition, the mold

[3]Model available at https://grabcad.com/library/helmet-184.

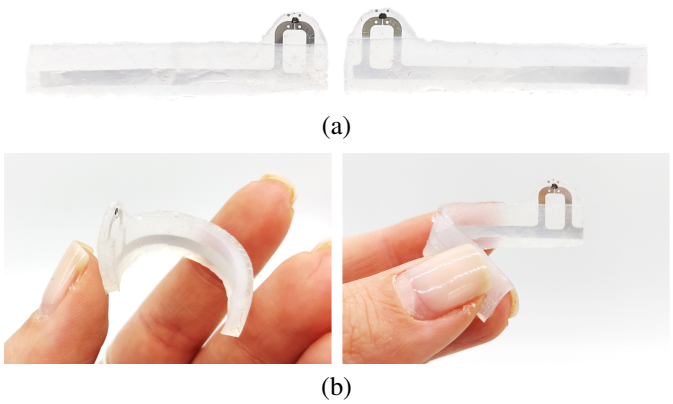

(a) (b)

Fig. 5. (a) Prototypes of the RFID sensor. (b) Evidence of the flexibility of the device.

(a) (b)

Fig. 6. (a) Volunteer wearing the dual-tag breath sensor on the prolabium, (b) in front of the reader antenna in a semi-anechoic room.

was placed in a climatic chamber (MKF 56 Binder GmbH [32]) at a temperature of $50°C$ and relative humidity of 25% for about 1 hour to foster polymerization. At the end of the process, the device was removed from the mold. It is compact, light, flexible, stretchable, and semi-transparent (Fig. 5.b). It can adhere to the skin without additional glue, can be cleaned with soap, and then applied again on the skin several times.

B. Electromagnetic Characterization

The electromagnetic performance of the on-skin device was measured by the Voyantic Tagformance station [33]. A volunteer wearing the breath sensors (Fig. 6.a) was accommodated in a semi-anechoic room, in sitting position. It was interrogated by the reference antenna of the TagFormance, which is a wideband linearly polarized (LP) reader antenna. It was placed $20\ cm$ away from the LP sensor antennas, at the nose height, with parallel polarization (Fig. 6.b). In real-life RFID installations, instead, circularly polarized (CP) patches are generally used so that the polarization efficiency will reduce to 0.5 with respect to the linear interrogating antenna in the most favorable alignment. To be conservative, this value is therefore assumed in the next estimations of the maximum read distances.

Starting from the measured turn-on power required to wake up each IC, Fig. 7 shows the corresponding broadband realized gains $\tilde{G}_{L/R}$, calculated as in [34]. Despite the small difference between the two tags, probably due to manufacturing

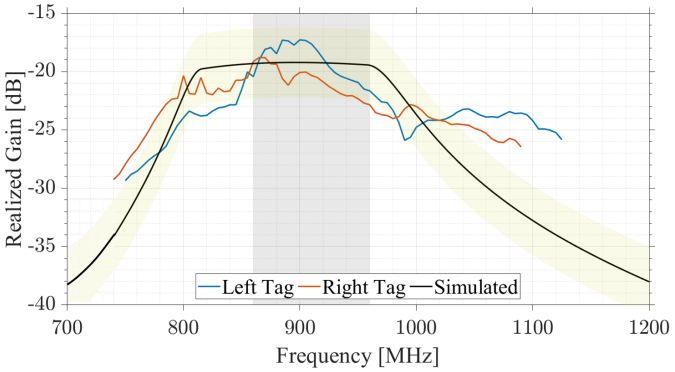

Fig. 7. Measured and simulated realized gains of the RFID antennas placed as in Fig. 6.b. The yellow band around simulated data indicates a $\pm 3\ dB$ uncertainty. Worldwide UHF band highlighted in grey.

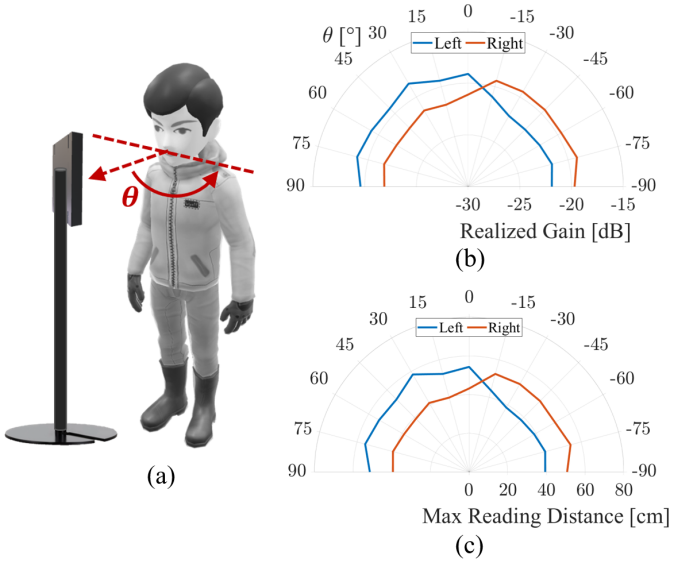

Fig. 8. (a) Schematic top view of the rotation of the volunteer with respect to the fixed antenna at a distance of $20\ cm$. (b) Measured realized gain at 870 MHz over the front half-space. (c) Estimation of the maximum reading distance, by assuming the reader emits the maximum allowed power of $3.2\ W\ EIRP$.

and placement imperfections, measurements are reasonably in agreement with the simulations, and hence the expected communication performance is confirmed. Moreover, keeping the antenna-sensors distance fixed, the interrogation angle was varied in the front half-space (Fig. 8.a), showing a fairly symmetrical behavior between the two sensors (Fig. 8.b) and stable performance. Fig. 8.c shows the corresponding estimation of the maximum reading distance, which is over $40\ cm$ in all the cases, by assuming a reader's power of $3.2\ W\ EIRP$ and a polarization loss factor of 0.5. [Reply to 3.4] Nevertheless, considering the threshold condition for temperature sensing (i.e., $PoC \geq 13$), the reading distance is reduced to $25\ cm$.

IV. Experimental Setup for Breath Monitoring

A. Instrumentation

The experimental set-up for bilateral breath monitoring by means of both the temperature-based sensors and the reference flow-meter is sketched in Fig. 9.

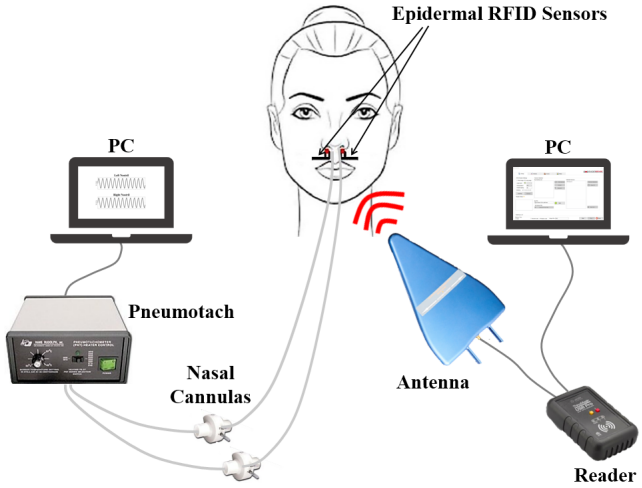

Fig. 9. Schematic representation of the measurement setup.

1) Dual-Tag Breath Sensor: The volunteers wore the epidermal breath sensor as in Fig. 6.a. The same LP interrogating antenna was this time connected to a low-cost RFID reader (ThingMagic USB Pro reader [35]) that is suitable to be easily carried and moved. The sampling rate was $f_s = 2\ Hz$ and the emitted power was $30\ dBm$, that, considering the gain of the reader antenna ($\sim 4.7\ dBi$ at 868 MHz), corresponds to approximately $3\ W\ EIRP$.

2) Reference Flow Meter: To record two distinct flow signals, each of the two nasal cannulas were inserted into a nostril and connected to an input channel of a reference flow meter consisting of a pneumotachograph (3700 series, non heated, 0-160 LPM, Hans Rudolph, Kansas City, MO, USA) combined with a differential pressure transducer (SensorTechnics, 144LU01D-PCB, Sensortechnics, Inc., Mansfield, CA, USA). The output signals from the two transducers were collected by a portable oscilloscope (PicoScope 4824, Pico Technology, UK) with a time window of $20\ s$, a sampling rate of $1.5\ kHz$, and a low-pass filter with a cut-off frequency of $2\ Hz$ [4] [36].

In all the tests reported next, temperature and airflow measurements were performed simultaneously.

It is worth noticing that, in such experimental setup, the nasal cannulas were inevitably affected by air leakage since their insertion into the nostrils was only partial so that part of the airflow could also pass over the temperature sensors. The detrimental effect of air leakage at the expense of flow signals is a well-known weak point of the flow meters [36]. It especially affects the dynamic range (i.e., the peaks) of the recorded signals, hence reducing their inspiratory and/or expiratory amplitude.

B. Breathing Guide

To emulate normal, as well as, pathological patterns, a metronome was used to guide the user through the execution of a mixed breathing pattern, with specific rates (Table I).

[4]The useful flow signal is preserved since a cut-off frequency of $2\ Hz$ is 4 times higher than the maximum respiratory frequency tested within the measurements campaign (i.e., $0.5\ Hz$). Whereas, at the same time, possible higher-frequency artifacts, due for example to involuntary movements or ambient air flows, are removed.

TABLE I
BREATHING PATTERNS

Breathing Type	Respiratory Rate	Frequency
Apnea	$0\ bpm$	–
Quiet Breathing	$15\ bpm$	$0.25\ Hz$
Deep Breathing	$15\ bpm$	$0.25\ Hz$
Tachypnea	$30\ bpm$	$0.50\ Hz$
Bradypnea	$8\ bpm$	$0.17\ Hz$

C. Set of Volunteers

The set of volunteers[5] for the experimental tests comprised 4 healthy persons, 2 males and 2 females ($25 \leq$ age ≤ 30, $1.55\ m \leq$ height $\leq 1.70\ m$, $43\ kg \leq$ weight $\leq 87\ kg$).

D. Characterization of Dual-Tag Breath Sensor Cross-Talk

The air flowing through one nostril during breathing can cause a disturbance at the expense of the temperature measurement performed at the other one. Such disturbance is evaluated in terms of the *cross-talk*[6] between the temperature data produced by the two ICs. The cross-talk matrix is:

$$\mathbf{\Theta}_{cross} = \begin{bmatrix} \Theta_{RR} & \Theta_{RL} \\ \Theta_{LR} & \Theta_{LL} \end{bmatrix}, \quad (4)$$

where $\Theta_{ij} = mean(|T_{ij} - mean(T_{ij})|)$, $i, j = \{L, R\}$. The subscript *"i"* indicates the measuring sensors while the subscript *"j"* the open nostril (whereas the other is kept fully obstructed). Hence, $\Theta_{ij}|_{i=j}$ provides an estimation of the temperature dynamics of the open nostril during breathing, whereas $\Theta_{ij}|_{i\neq j}$ gives a measurement of the cross-talk between sensors ($\Theta_{ij}|_{i\neq j} \rightarrow 0$ in the ideal case).

The cross-talk was preliminary evaluated by obstructing one nostril at a time and recording the temperature data from both the right and left sensors during a quiet breathing ($15\ bpm$) of a volunteer. Fig. 10 shows that the sensor under the open nostril recorded a distinguishable temperature profile, whereas the temperature sensor under the closed nostril mainly recorded noise and no clear profile is found. In this case, $\Theta_{RR} \approx \Theta_{LL} = 0.75\,^{\circ}C$ and $\Theta_{RL} \approx \Theta_{LR} = 0.13\,^{\circ}C$, so that the estimated cross-talk is less than the precision ($0.2\,^{\circ}C$) of the IC sensor. Hence, the measurements at the two nostrils can be considered as being independent.

V. PROCESSING PROCEDURES OF BREATH DATA

A. Data Framing and Equalization

The breathing traces of each volunteer are decomposed into 16 time-frames (size: $20\ s$), each corresponding to a different breathing phase. Overall, 92 couplets of respiration cycles are compared. The two raw datasets (temperature and airflow) are post-processed as follows.

[5]Volunteers were informed about the experiments and signed a written consent.

[6]In telecommunication, the *cross-talk* is a disturbance caused by one electromagnetic signal in a circuit affecting a signal in an adjacent circuit [37].

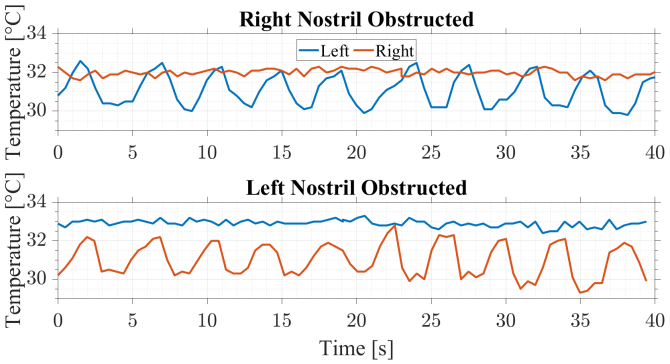

Fig. 10. Example of temperature trace, recorded during quiet breathing when one nostril at a time is obstructed.

(a) Flow Conversion - The voltage signals $F_i^V(t)$ returned by the flow meter are converted, by a calibration syringe device [36], into flow signals F_i as:

$$F_i\,[L/min] = \frac{50\,[1000\,F_i^V[V] - O_F(i)]}{1000},\ i = \{R, L\}, \quad (5)$$

where $O_F(R)$ and $O_F(L)$ are the offsets of the right and left nasal cannulas, respectively, evaluated by the companion software. As a result, both the flow traces oscillate around a null baseline. Then, the signals are down-sampled to $2\,Hz$ for a direct comparison with the temperature data.

(b) Temperature Offset and Drift Removal - Due to peculiar inter-IC manufacturing differences and to the user-dependent placement, the temperature profiles from different ICs could have different offsets (this is mostly evident during apnea). Accordingly, the next processing will refer to relative variations with respect to the apnea:

$$\Delta T_i = T_i - mean(T_i^{apnea}),\ i = \{R, L\}, \quad (6)$$

where $T_{R/L}^{apnea}$ are the temperature samples recorded from the right/left nostrils during approximately 20 seconds of apnea. Then, the resulting signals are processed with a first-order high-pass filter (cut-off frequency $f = 0.05\,Hz$ for bradypnea, and $f = 0.2\ Hz$ otherwise) to remove possible drifts related to the inertia of the IC sensors. As a result, also the L/R temperature traces now oscillate around a zero baseline.

An example of the raw respiratory patterns simultaneously recorded by the ICs and the flow meter is shown in Fig. 11. The emulated breathing waveforms are clearly distinguishable. For the sake of comparison, the rules rising=exhalation and falling=inhalation also apply here to flow signals, which are flipped with respect to the typical clinical convention to match the behavior of temperature signals. Even before the processing of the data, Fig. 11 shows the different behavior of the two nostrils, which is confirmed by the two instruments: both temperature and flow profiles of the right nostril are more pronounced than the left ones as a consequence of the natural asymmetry of the user's breathing.

Finally, Fig. 12 shows an example of bradypnea traces after the data processing. The asymmetric behavior of the two nostrils is well preserved.

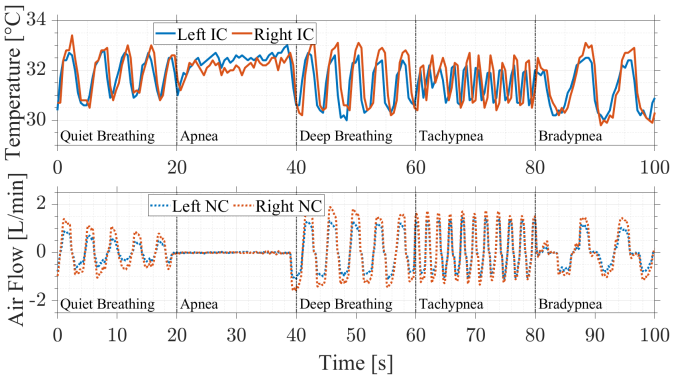

Fig. 11. Example of raw temperature and flow respiratory patterns recorded by the dual-tag ICs and by the nasal cannulas, performed by a volunteer.

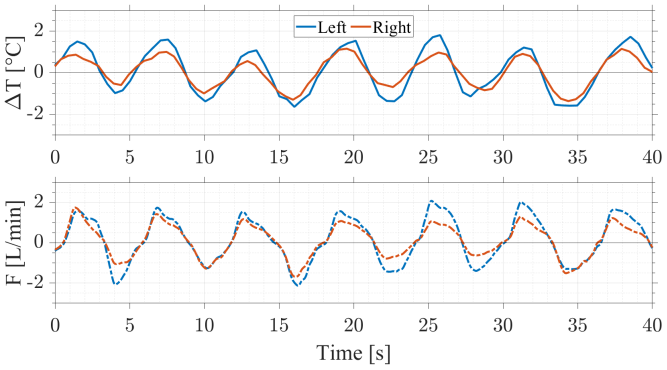

Fig. 12. Example of temperature and flow respiratory pattern after the data processing in the case of bradypnea.

B. Breathing Features

The following breathing features [38] are extracted to perform the comparison between the measurement instruments.

1) Inspiratory Time (IT) and Expiratory Time (ET): The inspiratory time (IT) and expiratory time (ET) are the time intervals during which the respiratory flow trace gets negative and positive, respectively (Fig. 13). They are key parameters in setting intensive care and anesthesia ventilators [39]. Computed IT and ET are averaged ($\overline{IT}$, $\overline{ET}$) over the periods of the time frame.

2) Respiratory Rate (RR): The respiratory rate (RR) corresponds to the number of breaths a person takes per minute. For each breathing pattern it is evaluated as:

$$RR = \frac{60}{\overline{IT} + \overline{ET}} \,. \tag{7}$$

3) Peaks Ratio (r): Peak Inspiratory Flow (PIF) and Peak Expiratory Flow (PEF) correspond to the minimum and the maximum of the respiratory trace, respectively (Fig. 13), and they characterize the overall dynamic range of the breathing pattern. They hence give information of the air flowing through the bronchi [40] and permit to identify the *degree of obstruction* in the airways. Equivalently, Peak Inspiratory Temperature (PIT) and Peak Expiratory Temperature (PET) can be defined as the minimum and maximum peaks of the temperature traces. Computed PIF, PEF, PIT, and PET are averaged over the periods of the time frames. Their ratios

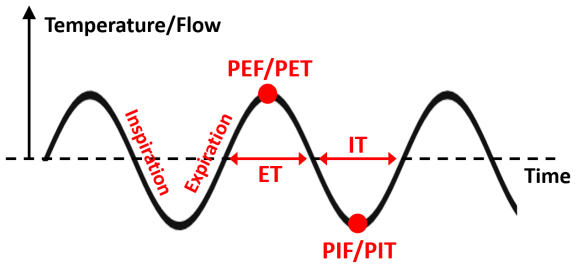

Fig. 13. Schematic indication of respiratory features.

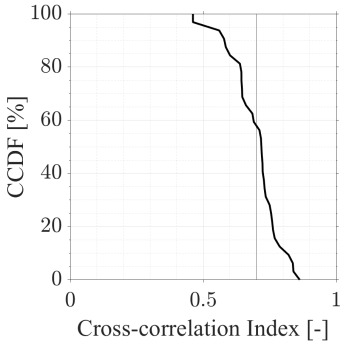

Fig. 14. Complementary Cumulative Distribution Function of cross-correlation indexes ρ for temperature-flow waveforms.

$r_F = PIF/PEF$ and $r_T = PIT/PET$ are expected to be independent on temperature and flow, and hence they can be calculated and compared.

4) L/R Peaks Ratio ($p_I^{L/R}$, $p_E^{L/R}$): The ratios between the peaks of left and right nostrils give an indication about congenital or permanent asymmetry of breathing (i.e., nasal septum deviation) or about the presence of possible temporary occlusion (i.e., flu, cold). The ratios are defined as:

$$p_Y^{L/R}\Big|_X = \frac{PIX^L}{PIX^R} \,,\; Y = \{I, E\} \,, \tag{8}$$

and are computed from flow ($X = F$) and temperature ($X = T$) signals to verify if the asymmetries detected by the flow meter are revealed also by the epidermal temperature sensor.

VI. Statistical Results

The comparative analysis of the above features is carried out by evaluating Cross-Correlation [41], Bland-Altman diagrams [42], and Cumulative Distribution Function (CDF) [43]. Temperature and flow outliers are discarded.

A. Temperature-Flow Correlation

The degree of correlation of the temperature-based breath measurement with the standard flow meter is quantified by means of the cross-correlation index $-1 < \rho < +1$ [41]. The more ρ is close to +1/-1, the maximum positive/negative correlation is present, whereas, if $\rho \simeq 0$, the two signals are uncorrelated. The cross-correlation index is computed for each couplet of temperature-flow frames. The corresponding indexes are cumulatively shown in Fig. 14 by means of the Complementary CDF (CCDF) diagram[7]. The cross-correlation

[7]Each point on the CCDF curve indicates the probability of having a correlation coefficient greater than or equal to the input abscissa [43].

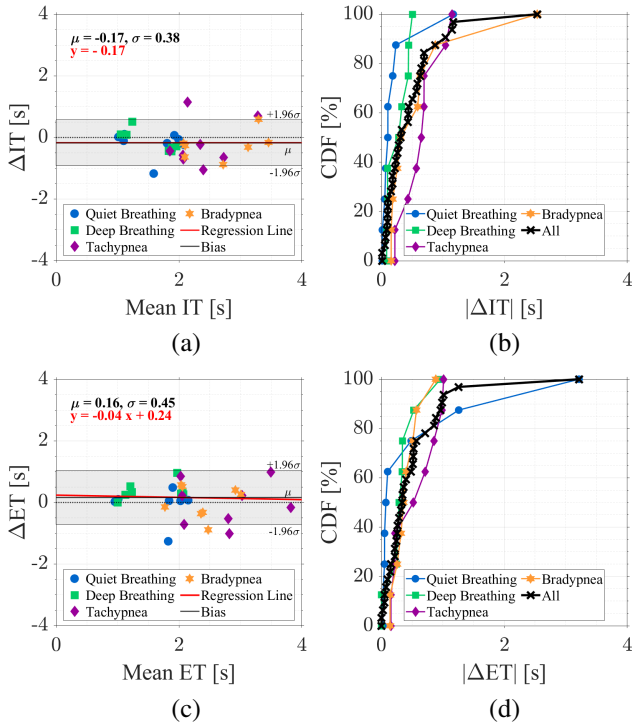

Fig. 15. Degree of agreement between the temperature and flow-based datasets for the $\boldsymbol{IT}$ and $\boldsymbol{ET}$ features. (a,c) Bland–Altman diagrams with indication of $\mathbf{95\%}$ limit of agreement, bias, standard deviation, and linear regression. (b,d) CFD plots for each breathing type, and for all the breathing types considered together.

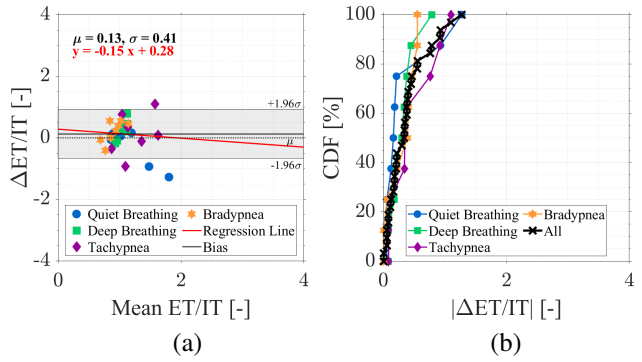

Fig. 16. Degree of agreement between the temperature and flow-based datasets for the $\boldsymbol{ET/IT}$ ratio. (a) Bland–Altman diagram and (b) CDF plots for each breathing type, and for all the breathing types considered together.

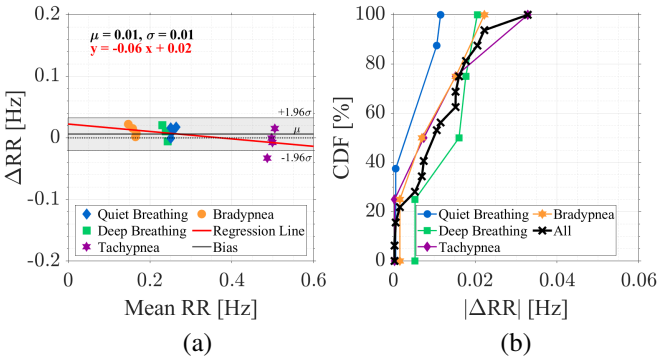

Fig. 17. Degree of agreement between the temperature and flow-based datasets for the respiration rate $\boldsymbol{RR}$. (a) Bland–Altman diagram and (b) CDF plots for each breathing type, and for all the breathing types considered together.

index is greater than 0.7 in 60% of cases, and greater than 0.5 in 95% of the cases. Therefore, the temperature measurement of breath is strongly correlated with the reference flow meter.

B. Comparative Analysis of Respiratory Features

1) Inspiratory Time (IT) and Expiratory Time (ET): Fig. 15 shows the results of the aggregated comparative analysis between the RFID temperature dataset and reference flow dataset concerning IT and ET features. Biases $\mu = \{-0.17, -0.16\}\, s$ and standard deviations $\sigma = \{0.38, 0.45\}\, s$ are derived from the Bland-Altman diagrams (Fig. 15.a,c), so that there is approximately less than $\pm 0.9\ s$ difference between the two measurement equipment within a 95% limit of confidence. Moreover, since the regression lines are nearly horizontal, the biases can be considered almost stable in the explored range. The plots of CDF[8] in Fig. 15.b,d show a better than $\pm 0.5\ s$ agreement in 60% of the cases, and better than $1\ s$ in 95% of the comparisons.

It is worth noticing that IT and ET span in the range 1–4 s according to the rhythms imposed by the metronome. But, since breathing was not natural (i.e., conditioned by the metronome), inspiratory and expiratory times are equally divided with respect to the duration of each breath, that is $IT \cong ET$. This is confirmed by the Bland-Altman diagram in Fig. 16.a that shows that ET/IT ratio gets values around unity, with a good flat bias ($\mu = 0.13$) between flow and temperature datasets, and with a difference of less than ± 0.5 in 80% of the cases (Fig. 16.b).

2) Respiratory Rate (RR): Fig. 17 shows the aggregated comparative analysis between temperature dataset and reference flow dataset concerning RR feature. The Bland-Altman diagram in Fig. 17.a returns a bias $\mu = 0.01 Hz$ and a standard deviation $\sigma = 0.01\ Hz$. Hence, there is a better $\pm 0.02\ Hz$ agreement within a 95% limit of confidence. This is confirmed by the CDF plot in Fig. 17.b. For each breathing pattern, the estimation difference is always less than $\pm 0.04\ Hz$, and even smaller in the case of quiet breathing, deep breathing, and bradypnea. Overall, a better than $\pm 0.02\, Hz$ agreement is obtained in the 80% of the comparisons.

3) Peaks Ratio (r): Fig. 18 shows the results of the aggregated comparative analysis concerning the peaks ratio r. Given that the analysis of respiratory times revealed that $IT \cong ET$, the same is expected for the peaks[9] (i.e., $PIF \cong PEF$ and $PIT \cong PET$), that means $r_F, r_T \cong 1$. The Bland-Altman diagram in Fig. 18.a returns a bias $\mu = -0.12$ and a standard deviation $\sigma = 0.17$, but the linear regression line shows a high slope, meaning that a proportional difference exists among the two datasets, and the difference between r_T and r_F is

[8]Each point on the CDF curve indicates the probability of having ΔRR values smaller than or equal to the input abscissa [43].

[9]For each respiratory act, the area underlying the inspiratory waveform is ideally (i.e., in the absence of leaks) equal to the expiratory area. Thus, if the times are the same (Fig. 16) and the shape of the waveforms is the same (Fig. 14), also the peaks are expected to be the same.

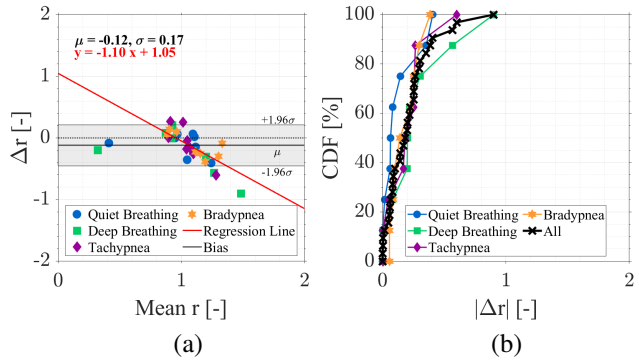

Fig. 18. Degree of agreement between the temperature and flow-based datasets for the peaks ratio r. (a) Bland–Altman diagram and (b) CDF plots for each breathing type, and for all the breathing types considered together.

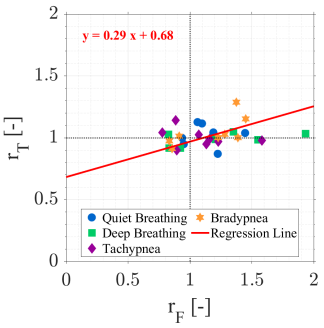

Fig. 19. Temperature peaks ratio data versus reference nasal cannulas with indication of linear regression.

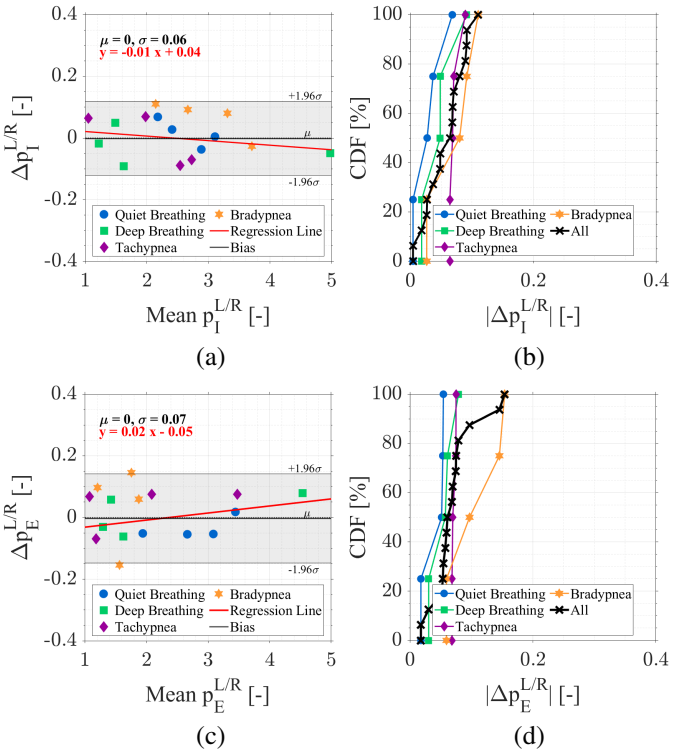

Fig. 20. Degree of agreement between the temperature and flow-based datasets for the $p_I^{L/R}$ and $p_E^{L/R}$ ratios. (a,c) Bland–Altman diagrams and (b,d) CDF plots for each breathing type, and for all the breathing types considered together.

consistent for values far from unity. To better investigate this behavior, the temperature peaks ratios r_T are plotted against the corresponding flow peaks ratios r_F in Fig. 19. Temperature data r_T are concentrated around the unitary ratio, as expected. Instead, the flow peaks ratio r_F exceeds unity as the presence of air leakage produces an imbalance between the inspiratory and expiratory areas underlying the flow waveform.

4) L/R Peaks Ratio ($p_I^{L/R}$, $p_E^{L/R}$): Fig. 20 shows the aggregated comparative analysis between temperature dataset and reference flow dataset concerning $p_I^{L/R}$ and $p_E^{L/R}$ ratios. Values of bias $\mu = \{0, 0\}$ and standard deviation $\sigma = \{0.06, 0.07\}$, derived from the Bland-Altman diagrams (Fig. 20.a,c), are remarkable. This means that the L/R asymmetry detected by the temperature is fully comparable to the one revealed by the flow, with an uncertainty of only ± 0.12. Also in this case the regression lines are nearly horizontal, hence the biases are almost stable in the explored range. The CDF plots in Fig. 20.b,d show a better $\pm 0.07\,\%$ agreement in 60% of the cases, and confirm that the uncertainty is less than ± 0.12 in 95% of the comparisons.

It is worth noticing (Fig. 20.a,c) that, on average, the values of ratios can span from 1 (= no asymmetry) up to 5 (= left nostril's peaks are 5 times bigger than right's) as a consequence of the volunteers' anatomy and their condition during the measurements.

VII. Summary and Conclusion

The paper has presented the evaluation of a dual-channel breath sensor, made of epidermal UHF RFID antennas, for the wireless temperature-based monitoring of the air flowing in and out of the nostrils. Thanks to soft and stretchable biocompatible elastomers, the device is soft, quite comfortable, self-adhesive, and reusable, avoiding unpractical wired instruments.

A measurement campaign investigated, for the first time, the clinical meaningfulness of features that can be derived from temperature-based signals with respect to the assessed spirometry. The comparative statistical analysis returned a good cross-correlation between the signals (better than 0.7 in 60% of the tests), and the prediction of temperature-based respiratory features deviates from the reference by less than 4–12% of the full scale (in the case of respiratory times). In particular, the respiratory rate can be predicted with an almost zero difference. Moreover, concerning the effect of air leakage, the proposed sensors revealed more robust than the flow meter, which is instead affected by air leaks from the nasal cannulas. This leakage, if not properly corrected [36], may alter the amplitude of the flow-meter signals, and hence the peak values. This relevant result must however be corroborated with further investigations.

The possibility of selective monitoring each nostril was also successfully demonstrated, with negligible cross-sensitivity of the temperature data recorded by the two ICs. In particular, the comparative analysis proved that the possible imbalance between the nostrils is properly detected by the sensor, with

an uncertainty of less than 10% compared to the reference.

Currently, the temperature-based method is not yet able to estimate the true value of the PIF and PEF, as well as the respiration volume. To this purpose, a temperature-flow calibration would be required, and this will the topic of future research. Nevertheless, the assessed capability to identify alterations in the breathing pattern (i.e., rhythm, relative depth) is yet compatible with real clinical application, especially in emergency scenarios such as field hospitals or in emerging Countries that have few resources and facilities for medical screenings. The RFID-based epidermal sensing could be moreover a game-changer for application in neonatal wards to monitor newborns by avoiding bounding wired instruments that currently preclude the vital physical contact between mother and baby.

Being a medical device, some of the critical points for a future certification in terms of regulation are biocompatibility, safety with respect to EM exposure, and accuracy and reproducibility of the sensed data. Some of these points have been partially addressed by this study since biocompatibility was achieved by using a skin-friendly material for coating, and the EM safety was verified by simulations. Moreover, the accuracy of the system is $0.2°C$ [24] and, as it works in a differential way, the possible miscalibration of the ICs will not affect the reproducibility.

REFERENCES

[1] A. Nicolo, C. Massaroni, E. Schena, and M. Sacchetti, "The Importance of Respiratory Rate Monitoring: From Healthcare to Sport and Exercise," *Sensors (Switzerland)*, vol. 20, pp. 1–45, November 2020.

[2] P. Loughlin, F. Sebat, and J. Kellet, "Respiratory Rate: The Forgotten Vital Sign - Make It Count!" *The Joint Commission Journal on Quality and Patient Safety*, vol. 44, June 2018.

[3] M. Woollard and I. Greaves, "Shortness of Breath," *Emergency medicine journal: EMJ*, vol. 21, May 2004.

[4] G. M. Bianco, C. Occhiuzzi, N. Panunzio, and G. Marrocco, "A Survey on Radio Frequency Identification as a Scalable Technology to Face Pandemics," *IEEE Journal of Radio Frequency Identification*, October 2021.

[5] J. Farman and D. Juett, "Impedance spirometry in clinical monitoring." *British Medical Journal*, vol. 4, pp. 27–29, October 1967.

[6] A. Aliverti, "Wearable technology: role in respiratory health and disease," *Breathe*, vol. 13, no. 2, pp. 27–36, June 2017.

[7] F. Guder, A. Ainla, J. Redston, B. Mosadegh, A. Glavan, T. J. Martin, and G. M. Whitesides, "Paper-Based Electrical Respiration Sensor," *Angewandte Chemie International Edition*, vol. 55, no. 19, pp. 5727–5732, April 2016.

[8] D. Toan, P. Hoang-Phuong, N. Tuan-Khoa, Q. Afzaal, P. Woodfield, Z. Yong, N. Nam-Trung, and D. Dzung Viet, "Solvent-free fabrication of biodegradable hot-film flow sensor for noninvasive respiratory monitoring," vol. 50, May 2017.

[9] Y.-F. Wang, T. Sekine, Y. Takeda, K. Yokosawa, H. Matsui, D. Kumaki, T. Shiba, T. Nishikawa, and S. Tokito, "Fully Printed PEDOT:PSS-based Temperature Sensor with High Humidity Stability for Wireless Healthcare Monitoring," *Scientific Reports*, vol. 10, February 2020.

[10] Y. Liu, L. Zhao, R. Avila, C. Yiu, T. Wong, Y. Chan, K. Yao, D. Li, Y. Zhang, W. Li, Z. Xie, and X. Yu, "Epidermal electronics for respiration monitoring via thermo-sensitive measuring," *Materials Today Physics*, vol. 13, p. 100199, June 2020.

[11] S. Milici, J. Lorenzo, A. Lazaro, R. Villarino, and D. Girbau, "Wireless Breathing Sensor Based on Wearable Modulated Frequency Selective Surface," *IEEE Sensors Journal*, vol. 17, no. 5, pp. 1285–1292, December 2016.

[12] P. Jiang, S. Zhao, and R. Zhu, "Smart Sensing Strip Using Monolithically Integrated Flexible Flow Sensor for Noninvasively Monitoring Respiratory Flow," *Sensors (Basel, Switzerland)*, vol. 15, December 2015.

[13] D.-H. Kim, N. Lu, R. Ma, Y.-S. Kim, R.-H. Kim, S. Wang, J. Wu, S. Won, H. Tao, A. Islam, K. Yu, T.-i. Kim, R. Chowdhury, M. Ying, L. Xu, M. li, H.-j. Chung, H. Keum, M. McCormick, and J. Rogers, "Epidermal Electronics," *Science*, vol. 333, pp. 838–43, August 2011.

[14] M. C. Caccami, M. Y. Mulla, C. Di Natale, and G. Marrocco, "Graphene oxide-based radiofrequency identification wearable sensor for breath monitoring," *IET Microwaves, Antennas & Propagation*, vol. 12, no. 4, pp. 467–471, February 2018.

[15] M. C. Caccami, M. Y. S. Mulla, C. Occhiuzzi, C. Di Natale, and G. Marrocco, "Design and Experimentation of a Batteryless On-Skin RFID Graphene-Oxide Sensor for the Monitoring and Discrimination of Breath Anomalies," *IEEE Sensors Journal*, vol. 18, no. 21, pp. 8893–8901, August 2018.

[16] C. Occhiuzzi, M. C. Caccami, S. Amendola, and G. Marrocco, "Breath-monitoring by means of Epidermal Temperature RFID Sensors," in *2018 3rd International Conference on Smart and Sustainable Technologies (SpliTech)*, August 2018, pp. 1–4.

[17] C. Miozzi, G. Stendardo, G. M. Bianco, F. Montecchia, and G. Marrocco, "Dual-chip RFID On-skin Tag for Bilateral Breath Monitoring," in *2021 IEEE International Conference on RFID (RFID)*, April 2021, pp. 1–6.

[18] E. Fontana, N. Panunzio, F. Montecchia, and G. Marrocco, "Two-channel Epidermal RFID Sensor for the Analysis of Nasal Respiratory Flow," in *2022 16th European Conference on Antennas and Propagation (EuCAP)*, April 2022, pp. 1–5.

[19] N. Panunzio and G. Marrocco, "A Multi-port Formulation for Electromagnetic Coupled Auto-tuning RFID Antennas," in *2021 XXXIVth General Assembly and Scientific Symposium of the International Union of Radio Science (URSI GASS)*, October 2021, pp. 1–4.

[20] M. C. Caccami and G. Marrocco, "Electromagnetic Modeling of Self-Tuning RFID Sensor Antennas in Linear and Nonlinear Regimes," *IEEE Transactions on Antennas and Propagation*, vol. 66, no. 6, pp. 2779–2787, March 2018.

[21] R. Micron, https://axzon.com/rfm3200-wireless-flexible-temperature-sensor/, October 2021.

[22] A. Dharap, A. H. Salem, R. Fadel, M. Osman, M. Chakravarty, N. Latif, and M. Abu-Hijleh, "Facial Anthropometry in an Arab Population," *Bahrain Medical Bulletin*, vol. 35, pp. 69–73, June 2013.

[23] Axzon, "RFM3300-E Magnus-S3 M3E passive sensor IC," https://axzon.com/rfm3300-e-magnus-s3-m3e-passive-sensor-ic/, September 2021.

[24] F. Camera and G. Marrocco, "Electromagnetic-Based Correction of Bio-Integrated RFID Sensors for Reliable Skin Temperature Monitoring," *IEEE Sensors Journal*, vol. 21, no. 1, pp. 421–429, August 2021.

[25] G. Marrocco, "RFID Grids: Part I - Electromagnetic Theory," *IEEE Transactions on Antennas and Propagation*, vol. 59, no. 3, pp. 1019–1026, January 2011.

[26] S. Amendola and G. Marrocco, "Optimal Performance of Epidermal Antennas for UHF Radio Frequency Identification and Sensing," *IEEE Transactions on Antennas and Propagation*, vol. 65, no. 2, pp. 473–481, December 2016.

[27] ETSI EN 300 220-2 V3.2.1 (2018-06), "Short Range Devices (SRD) operating in the frequency range 25 MHz to 1000 MHz," https://axzon.com/rfm3300-e-magnus-s3-m3e-passive-sensor-ic/, December 2021.

[28] "1999/519/EC: Council Recommendation of 12 July 1999 on the limitation of exposure of the general public to electromagnetic fields (0 Hz to 300 GHz)," https://op.europa.eu/it/publication-detail/-/publication/9509b04f-1df0-4221-bfa2-c7af77975556/language-en, November 2021.

[29] G. M. Bianco, N. Panunzio, and G. Marrocco, "RFID Research Against COVID-19 - Sensorized Face Masks," in *2021 IEEE International Conference on RFID Technology and Applications (RFID-TA) (IEEE RFID-TA 2021)*, October 2021.

[30] N. Panunzio, C. Occhiuzzi, and G. Marrocco, "Propagation Modeling Inside the International Space Station for the Automatic Monitoring of Astronauts by Means of ¡italic¿Epidermal¡/italic¿ UHF-RFID Sensors," *IEEE Journal of Radio Frequency Identification*, vol. 5, no. 2, pp. 174–181, February 2021.

[31] F. Naccarata, G. M. Bianco, and G. Marrocco, "Multi-Channel Radiofrequency Finger Augmentation Device for Tactile Internet," in *2021 XXXIVth General Assembly and Scientific Symposium of the International Union of Radio Science (URSI GASS)*, October 2021, pp. 1–4.

[32] Binder, https://www.binderworld.com/en/products/ dynamic-climate-chambers/series-mkf/mkf-56, October 2021.

[33] Voyantic, "Tagformance Pro," https://voyantic.com/products/tagformance-pro, September 2021.

[34] N. Panunzio, F. Ciafrei, C. Magnante, G. M. Bianco, and G. Marrocco, "Sensorized Facemask with Temperature RFID Sensor for Cough Analysis," in *2022 16th European Conference on Antennas and Propagation (EuCAP)*, April 2022, pp. 1–5.
[35] Jadak, "ThingMagic USB Pro UHF Reader," https://www.jadaktech.com/products/thingmagic-rfid/thingmagic-usb-pro-uhf-reader/, October 2021.
[36] F. Montecchia, F. Midulla, and P. Papoff, "A flow-leak correction algorithm for pneumotachographic work-of-breathing measurement during high-flow nasal cannula oxygen therapy," *Medical engineering physics*, vol. 54, February 2018.
[37] J. Price and T. Goble, "10 - Signals and noise," in *Telecommunications Engineer's Reference Book*, F. Mazda, Ed. Butterworth-Heinemann, 1993, pp. 10–1–10–15.
[38] M. J. Parker, "Interpreting Spirometry: The Basics," *Otolaryngologic Clinics of North America*, vol. 47, no. 1, pp. 39–53, February 2014.
[39] S. Ahmed and M. Athar, "Mechanical ventilation in patients with chronic obstructive pulmonary disease and bronchial asthma," *Indian Journal of Anaesthesia*, vol. 59, pp. 589–598, September 2015.
[40] W. Janssens, P. VandenBrande, E. Hardeman, E. Langhe, T. Philps, T. Troosters, and M. Decramer, "Inspiratory flow rates at different levels of resistance in elderly COPD patients," *The European respiratory journal : official journal of the European Society for Clinical Respiratory Physiology*, vol. 31, pp. 78–83, February 2008.
[41] T. R. Derrick and J. M. Thomas, "Time Series Analysis: The Cross-Correlation Function," *Kinesiology Publications*, vol. 46, January 2004.
[42] D. Giavarina, "Understanding Bland Altman analysis," *Biochemia Medica*, vol. 25, pp. 141–151, June 2015.
[43] A. Clauset, C. Shalizi, and M. Newman, "Power-Law Distributions in Empirical Data," *SIAM Review*, vol. 51, June 2007.

Nicoletta Panunzio received the B.S. and M.S. degree in Medical Engineering (Hons.) from the University of Rome Tor Vergata, Rome, Italy in 2017 and 2020, respectively. She is currently pursuing the Ph.D. degree in Computer Science, Control and Geoinformation within the Pervasive Electromagnetics Lab at the University of Rome Tor Vergata, Rome, Italy.

She is a Student Member of IEEE since 2021. Her research interests include on-skin flexible antennas for smart health monitoring and detection of biophysical parameters, with particular interest in innovative multi-point systems to strengthen sensing accuracy and enable multi-parametric sensing.

Ms. Panunzio serves as a teaching tutor in two courses within the Medical Engineering school (Mechanics of Biological Systems and Wearable Systems and Medical Telemetry), and as a delegate professor in a course within the Engineering Sciences school (Electromagnetic Fields). Ms. Panunzio's awards and honors include the Best Student Paper Award (2021 IEEE International Conference on RFID Technology and Applications) and the Best Paper Award (2022 7th International Conference on Smart and Sustainable Technologies).

Elisa Fontana was born in Rome in 1995. She received the M.S. degree in Medical Engineering from the University of Rome Tor Vergata, Rome, Italy in 2021 with a Master thesis about differential breath measurements to determine respiratory flow temperature. She is currently with the Microwave Research Group at the University of Rome Tor Vergata, Rome, Italy where she is developing a microwave tomograph for the analysis of archaeological assets. The project is in collaboration with the National Research Council of Italy (PI of the project).

Francesco Montecchia was born in Italy in 1960. He received a degree in Electronic Engineering ("Electromagnetics") from the University of Ancona, Ancona, Italy in 1986, with an experimental thesis on "Microstrip-Antenna design for Hyperthermia treatments of superficial tumors". He received a specialist degree from the Postgraduate School of Health Physics of the University of Rome Tor Vergata, Rome, Italy in 1991.

From 1986 to 1992 he was employed at the Medical Physics Division of the University of Rome Tor Vergata where he carried out research concerning the design, development, and evaluation of RF/MW applicators and apparatuses for experimental and clinical hyperthermia treatments of superficial and subcutaneous tumors. From 1992 to today he has been engaged at the Physics and Bioengineering Institute of the University of Urbino, Urbino, Italy, the Neonatal and Pediatric Intensive Care Divisions of Sapienza University of Rome, the Anesthesia Division of Campus Bio-Medico University of Rome, and Medical Physics, Anesthesia Divisions, and Civil Engineering & Computer Science Engineering Department of the University of Rome Tor Vergata in the research, design, development, and optimization of advanced lung ventilation systems and of innovative devices and algorithms for diagnostic and therapeutic evaluation of breathing assistance. Since 2008 he has been the head of the Medical Engineering Laboratory of the University of Rome Tor Vergata.

From 1990 to today he has been a Lecturer in Physics, Medical & Health Physics, Biophysics and Biomedical Engineering Instrumentation at the Universities where he is involved in the research.

Gaetano Marrocco received the M.S. degree in Electronic Engineering and Ph.D. degree in Applied Electromagnetics from the University of L'Aquila, L'Aquila, Italy in 1994 and 1998, respectively. He was a Researcher at the University of Rome Tor Vergata, Rome, Italy from 1994 to 2014. He was an Associate Professor of Electromagnetics from 2013 to 2017, and a Full Professor at the University of Rome Tor Vergata since 2018. He currently serves as Director of the Medical Engineering School.

The first phase of his career was devoted to the research on Time-Domain Electromagnetics with application to structural, broadband, and ultra-wideband antennas for Satellite (ESA, ASI), Avionic, and Naval (Leonardo) communications. Then, since 2002, he is investigating sensor-oriented miniaturized antennas for Biomedical Engineering and Radiofrequency Identification (RFID), contributing to the move from the RF labeling of objects to the passive sensor networks in the Internet of Things era. He carried out pioneering research on body-centric battery-less wireless sensors concerning textile RFID antennas, tattoo-like sensors (flexible and stretchable epidermal electronics), and radio-sensors embedded inside implanted prostheses.

He serves as Associate Editor for the IEEE Journal of Radiofrequency Identification and for the IEEE Journal of Flexible Electronics and was a member of the IEEE Antennas and Propagation Society Awards committee. Moreover, he is the chair of the Italian delegation URSI Commission D Electronics and Photonics. He was the chair of the Local Committee of the V European Conference on Antennas and Propagation (EUCAP-2011), TPC chair of the 2012 IEEE-RFID TA in Nice, France, TPC track-chair of the 2016 IEEE Antennas and Propagation Int. Symposium, TPC track-chair of IEEE-RFID 2018-22, USA.

Prof. Marrocco is the director of the Pervasive Electromagnetics Lab (www.pervasive.ing.uniroma2.it) and the co-founder and president of the University spin-off RADIO6ENSE (www.radio6ense.com), which is active in the short-range electromagnetic sensing for the Industrial Internet of Things, Smart Manufacturing, Automotive and Medical Device.

He is listed in the PLOS ranking of Top 2% Scientists Worldwide (source Univ. Stanford, 2022).